The influence of the trans-ligand to NO on the thermal stability of the photoinduced side-bond coordinated linkage isomer

Artem Mikhailov, Gennadiy Kostin, Dominik Schaniel

▶ **To cite this version:**

Artem Mikhailov, Gennadiy Kostin, Dominik Schaniel. The influence of the trans-ligand to NO on the thermal stability of the photoinduced side-bond coordinated linkage isomer. New Journal of Chemistry, 2022, 46 (26), pp.12641-12650. 10.1039/D2NJ01388F . hal-03826183

HAL Id: hal-03826183
https://hal.univ-lorraine.fr/hal-03826183v1

Submitted on 24 Oct 2022

HAL is a multi-disciplinary open access archive for the deposit and dissemination of scientific research documents, whether they are published or not. The documents may come from teaching and research institutions in France or abroad, or from public or private research centers.

L'archive ouverte pluridisciplinaire **HAL**, est destinée au dépôt et à la diffusion de documents scientifiques de niveau recherche, publiés ou non, émanant des établissements d'enseignement et de recherche français ou étrangers, des laboratoires publics ou privés.

The influence of *trans*-ligand to NO on the thermal stability of photoinduced side-bond coordinated linkage isomer

Artem A. Mikhailov[a], Gennadiy A. Kostin[a], Dominik Schaniel[b]

[a] Nikolaev Institute of Inorganic Chemistry, Siberian Branch of the Russian Academy of Sciences, 3 Acad. Lavrentiev Avenue, Novosibirsk 630090, Russian Federation

[b] Université de Lorraine, CNRS, CRM2, UMR 7036, Nancy 54000, France

Abstract

The influence of *trans*-to NO ligand (**X**) on the thermal stability of transient side-on coordinated nitrosyl linkage isomer (MS2) is investigated in a series of *trans*-[RuNOPy$_4$X](PF$_6$)$_2$ (X = F$^-$ (**RuF**), Cl$^-$ (**RuCl**), Br$^-$ (**RuBr**) and OH$^-$ (**RuOH**)) compounds. Based on differential scanning calorimetry (DSC) and IR-spectroscopy investigations, activation energies (E_a) and frequency factors (k_0) are determined for MS1→GS and MS2→GS reactions. Calculated decay temperatures (T_d) of both processes correlate with Mulliken electronegativities of **X** and Hirshfeld charges of the (RuNO) unit, the increase in the electronegativity of **X** or in the positive charge on the (RuNO) group leads to an increase in thermal stability of the MS2 isomer with almost linear dependence. Since the MS2 isomer is a transient state in MS1 isomer formation or NO release reaction, the obtained correlation can be used for the design of compounds with higher quantum yields of these processes.

Introduction

Linkage isomerism is a property of a wide family of coordination compounds with ligands such as sulfoxides (SO) [1–3], dinitrogen (N_2) [4,5], nitrite (NO_2) [6–9] and nitrosyl (NO) [10,11]. The isomerization in these compounds is often accessible only by light excitation, thereby providing means for controlled reversible molecular switching that can be applied for data storage or sensors technologies [12–15]. Moreover, light activation of such complexes in solutions (especially in case of NO compounds) could result in a release of free small molecules and can be used in photodynamic therapy for target drug delivery [16,17].

For the nitrosyl compounds at least three types of NO coordination are known: M-NO (GS), M-ON (metastable state 1, MS1) and M-η^2-(NO) (MS2, side bond). This diversity of coordination modes gives rise to a relatively complicated mechanism of NO photo-isomerization. Experimentally it was shown that the generation of MS1 can be described as a two-step process GS→MS2→MS1 with participation of two photons of the same wavelength, typically in the blue-green spectral range [18,19], and that MS2 can then be obtained by back transfer from MS1 using infrared light [20]. Recent calculations reveal that the isomerization occurs most probably via triplet states formation in case of all isomers, even though purely internal conversion processes are also possible [21–23]. Furthermore, again according to recent calculations, MS2 is supposed to be involved as an intermediate state in the mechanism of photorelease of nitric oxide [24,25]. Thus, the side-bond isomer MS2 plays a crucial role as an intermediate state

towards MS1 formation or NO release, where longer lifetime of MS2 increases both probability of MS1 formation and quantum yield of nitric oxide release.

Nevertheless, the structure-property correlations linking the thermal stability of MS2 to the properties of the metal center and its coordination sphere are absent in literature. In general, there are several obstacles to investigate the properties of MS2: i) a much lower thermal stability of MS2 with respect to MS1, which forces researchers to use additional cooling or time-resolved methods [26]; ii) a low population of generated MS2 isomers, which only in exceptional cases reaches 48% [27]; iii) a special photo-generation protocol is required to sufficiently populate MS2 via subsequent irradiation of MS1 by infrared light [28]; iv) the absence of known synthetic approaches for the preparation of series of complexes with similar counterions and different *trans*-ligands to NO.

Earlier, linkage isomers MS1 and MS2 were extensively studied in pyridine (Py) complex *trans*-$[RuNOPy_4Cl](PF_6)_2 \cdot 0.5H_2O$ (**RuCl**). By IR-, UV-vis spectroscopy and X-Ray diffraction the highest achieved population of MS1 (92%) and MS2 (48%) for the complex was established and thermal stability of both isomers was determined [20,27]. Later, a high population of both isomers was shown in *trans*-$[RuNOPy_4Br](PF_6)_2$ (**RuBr**) complex and authors concluded that pyridine ligands and PF_6^- counterions favor a high population of linkage isomers [29]. However, only IR-spectra of linkage isomers in **RuBr** compound were reported. The data on thermal stability of linkage isomer MS1 in *trans*-$[RuNOPy_4OH](PF_6)_2$ (**RuOH**) were reported by Coppens [11]. Nevertheless, particular kinetic parameters (activation energy and frequency factor) of the decay of MS1 were not presented. Taken into account the relatively high population of MS1 and MS2, the complexes with formula *trans*-$[RuNOPy_4X](PF_6)_2$ (**X** - ligand in *trans*-position to NO) are attractive species for the investigation of thermal properties of MS2 and the evaluation of *trans*-ligand influence.

In order to investigate the influence of *trans*-**X** ligand to the properties of photo-generated isomer MS2, a series of *trans*-$[RuNOPy_4X](PF_6)_2$ ($X = F^-$ (**RuF**), Cl^- (**RuCl**), Br^- (**RuBr**) and OH^- (**RuOH**)) compounds was prepared. The spectroscopic and thermal properties of the photogenerated linkage isomers were investigated by combined UV-vis, IR-spectroscopy and differential scanning calorimetry (DSC). Additional DFT calculations revealed a correlation of metastable states' thermal stability with the Hirshfeld charges of the compounds.

Experimental

Synthesis of *trans*-$[RuNOPy_4OH](PF_6)_2 \cdot H_2O$ (RuOH)

The starting complex *fac*-$[RuNOPy_2Cl_3]$ was prepared using the method described earlier [30]. Pyridine (60 ml) was added to a solution of *fac*-$[RuNOPy_2Cl_3]$ (2.88 g) in 500 ml of water and the mixture was heated with mixing at ≈100 C° in a closed beaker during 15 min. During the heating, the solution turned color from purple to orange. Then, the solution was cooled down to room temperature and filtered from a small amount of insoluble pale purple residue. The resulting solution was evaporated to obtain a wet deep orange solid. The solid was dissolved in 20 ml of water and mixed with 2.8 g of KPF_6. A yellow powder of $[RuNOPy_4OH](PF_6)_2 \cdot H_2O$ was readily precipitated and filtered on a glass filter, washed with diethyl ether. The yield of the *trans*-$[RuNOPy_4OH](PF_6)_2 \cdot H_2O$ is 53% (2.92 g). The powder

XRD patterns of the bulk sample correspond to the theoretical patterns calculated from the available crystal structure data determined by single-crystal XRD [31]. IR bands at room temperature, cm^{-1}: 3651, 3579, 3396 [ν(O-H)]; 3128 [ν(N-H)]; 1867 [ν(NO)]; 1612, 1455, 1222, 1072, 1020, 763, 689 [pyridine rings]; 837 [ν(P-F)]; 557 [δ(F-P-F)].

Synthesis of *trans*-[RuNOPy$_4$Cl](PF$_6$)$_2$·0.5H$_2$O (RuCl) and *trans*-[RuNOPy$_4$Br](PF$_6$)$_2$ (RuBr)

To the yellow powder of the parent complex [RuNOPy$_4$OH](PF$_6$)$_2$·H$_2$O (0.2 g) the corresponding amount of concentrated acid (HCl, HBr) (5-20 ml) was added. The mixture was gently heated with mixing at ≈60 C° in a closed beaker during 1 h. The resulting solution was evaporated several times with water at room temperature in order to remove acid residue. Finally, obtained orange residue (deep orange in case of *trans*-[RuNOPy$_4$Br](PF$_6$)$_2$) was dissolved in a minimum volume of water and mixed with 0.1 g of KPF$_6$. The powder was readily precipitated and filtered on a glass filter, washed with diethyl ether. The yield of the *trans*-[RuNOPy$_4$Cl](PF$_6$)$_2$·0.5H$_2$O or *trans*-[RuNOPy$_4$Br](PF$_6$)$_2$ is 85% (≈0.18 g). The powder XRD patterns of the bulk samples correspond to the theoretical patterns calculated from the available crystal structure data determined by single-crystal XRD [29,32]. IR bands at room temperature of *trans*-[RuNOPy$_4$Cl](PF$_6$)$_2$·0.5H$_2$O, cm^{-1}: 3638, 3576, 3432 [ν(O-H)]; 3128 [ν(N-H)]; 1911 [ν(NO)]; 1612, 1455, 1225, 1073, 1019, 758, 695 [pyridine rings]; 836 [ν(P-F)]; 558 [δ(F-P-F)]. IR bands at room temperature of *trans*-[RuNOPy$_4$Br](PF$_6$)$_2$, cm^{-1}: 3127 [ν(N-H)]; 1901 [ν(NO)]; 1612, 1454, 1225, 1072, 1019, 756, 696 [pyridine rings]; 837 [ν(P-F)]; 558 [δ(F-P-F)].

Synthesis of *trans*-[RuNOPy$_4$F](PF$_6$)$_2$·0.33H$_2$O (RuF) and *trans*-[RuNOPy$_4$F](PF$_6$)$_2$·1.5CH$_3$CN

The starting complex *trans*-[RuNOPy$_4$F](ClO$_4$)$_2$ was obtained using the method described earlier [33]. To solution of *trans*-[RuNOPy$_4$F](ClO$_4$)$_2$ (51 mg) in minimum volume of water was added water solution of NaPF$_6$ (26 mg). The resulting solution was evaporated at room temperature until yellow crystals were formed. The crystals were filtered on a glass filter and washed with diethyl ether. The yield of *trans*-[RuNOPy$_4$F](PF$_6$)$_2$·0.33H$_2$O is 73%. A slow evaporation of the water solution of the complex gave plate-shaped crystals of *trans*-[RuNOPy$_4$F](PF$_6$)$_2$·0.33H$_2$O suitable for X-ray diffraction analysis. A slow diffusion of diethyl ether into a solution of the complex in acetonitrile gave needle-shaped crystals of *trans*-[RuNOPy$_4$F](PF$_6$)$_2$·1.5CH$_3$CN, which structure was also determined by X-ray diffraction. Only one single crystal of *trans*-[RuNOPy$_4$F](PF$_6$)$_2$·1.5CH$_3$CN was selected for XRD measurement, since the compound is not stable without solution. The powder XRD patterns of both bulk samples correspond to the theoretical patterns calculated from crystal structure data of *trans*-[RuNOPy$_4$F](PF$_6$)$_2$·0.33H$_2$O complex determined by single-crystal XRD, indicates complex with captured acetonitrile molecules is stable only in solution. Elemental analysis for $Ru_1N_5O_{1.3}C_{20}H_{20.7}F_{13}P_2$, calculated/found (%): H 2.7/2.5, N 9.2/8.9., C 31.5/31.6. IR bands at room temperature, cm^{-1}: 3660, 3586, 3448 [ν(O-H)]; 3127 [ν(N-H)]; 1914, 1894 [ν(NO)]; 1614, 1456, 1224, 1073, 1020, 760, 691 [pyridine rings]; 837 [ν(P-F)]; 557 [δ(F-P-F)].

Single-crystal X-Ray diffraction

Single crystal X-ray diffraction data of complexes *trans*-[RuNOPy$_4$F](PF$_6$)$_2$·0.33H$_2$O and *trans*-[RuNOPy$_4$F](PF$_6$)$_2$·1.5CH$_3$CN were collected on a Bruker Apex Duo diffractometer with CCDs using graphite-

monochromated MoKα radiation (λ = 0.71073 Å) via 0.5° ω- and ϕ-scan techniques. Reduction of the experimental data was performed using the APEX2 suite. The structures were solved by SHELXT and refined by the full-matrix least-squares technique SHELXL [34] assisted with the Olex2 GUI [35]. The atomic displacement parameters of the ordered non-H atoms were refined using an anisotropic approximation except disordered units. The hydrogen atoms of the pyridine ligands were located geometrically and refined using the riding model. Crystallographic characteristics, experimental data, and the structure refinements are listed in Table S1. The structures of *trans*-$[RuNOPy_4F](PF_6)_2 \cdot 1.5CH_3CN$ and *trans*-$[RuNOPy_4F](PF_6)_2 \cdot 0.33H_2O$ have been deposited with the CCDC with deposition numbers 2143051 and 2143052, respectively.

IR- and UV-vis-spectroscopy

IR-spectroscopy measurements with irradiation were performed using a Nicolet 5700 FT-IR spectrometer with a resolution of 2 cm^{-1} in the range 400–4000 cm^{-1}. The sample (around 1-2 mg) was mixed with KBr (around 100 mg) and pressed into common pellets for IR measurements. The pellets were bonded onto the cold finger of a closed-cycle cryostat (Oxford Optistat) allowing to control the temperature in range 10 - 300 K. The irradiation procedures were performed by Thorlabs LEDs (Light Emitting Diodes) through KBr windows perpendicular to the samples with light of different wavelengths (365 – 1050 nm) with 50 - 200 mW optical power. To investigate the isothermal kinetics of MS2 decay in **RuOH** and **RuBr** the following protocol was applied: on the first stage the sample was irradiated at 80 K by chosen blue light in order to generate a sufficient amount of MS1 isomer; on the second stage obtained MS1 was irradiated at the same temperature by chosen infrared light in order to generate MS2; then the temperature was increased up to chosen value and then repeated measurement (the delay between spectra was 90 or 120 s) was performed in isothermal mode. Further, activation energy and frequency factors were determined in Arrhenius coordinates (Fig. S5). UV-vis spectra were recorded using transparent KBr pellets with the complex via a Varian CARY 4000 spectrometer. The transparent pellets were prepared and irradiated as for the IR measurements. Low-temperature measurements were performed using the same cryostat as that for the IR measurements, except that the KBr windows were exchanged for standard borosilicate glass windows. The baseline was measured using the same diaphragm with a KBr pellet, which can be mounted on the cryostat sample holder.

Differential scanning calorimetry

Differential scanning calorimetry (DSC) experiments were performed on a Mettler–Toledo DSC1 instrument equipped with a high-sensitivity DSC HSS8 sensor. The sample (1-5 mg of the powder) was homogeneously spread in a standard aluminum crucible (40 ml), such that it formed a thin layer covering the whole surface of the crucible. For MS1 generation, irradiation of GS was performed at 143 K for 20 min through a glass window, using chosen LED light similar to IR measurement. MS2 was generated at the same temperature by two-step irradiation as for IR measurements. To detect the enthalpy release during thermal relaxation of the metastable states, the sample was then heated from 143 to 353 K at a heating rate of 9 K min^{-1}. As a reference measurement the sample was measured

using the same protocol but without light irradiation. The experimental data were processed using the Netzsch Proteus analysis software.

DFT calculations

Density functional theory calculations of **RuF**, **RuCl**, **RuBr** and **RuOH** in GS, MS1 and MS2 ($[RuNOPy_4X]^{2+}$ in gas phase) were performed in ADF2020 package [36]. For geometry optimization of GS initial geometries were taken from available XRD structural data [29,31,32], for MS1 and MS2 geometry optimization available XRD data of linkage isomers in **RuCl** were used [27]. BP86 functional (including the local exchange expression correction by Becke and the local correlation correction by Perdew) [37] with triple-ζ-quality with one polarization function (TZP) basis set and Spin-Orbit coupling were used.

Results and discussion

Description of *trans*-$[RuNOPy_4F](PF_6)_2 \cdot 0.33H_2O$ (RuF) structure

In order to shine light on the influence of *trans*-ligand to the spectroscopic and thermal stability properties of NO linkage isomers, PF_6^- salts of *trans*-$[RuNOPy_4X]^{2+}$ cations ($X = F^-, Cl^-, Br^-, OH^-$) were prepared. The crystal structures of salts with $X = Cl^-$, Br^- and OH^- were reported earlier [29,31,32], whereas PF_6^- structure of the fluoride complex is reported here for the first time and described below. It should be mentioned that *trans*-$[RuNOPy_4X]^{2+}$ ($X = Cl^-$, Br^-, OH^-) compounds can be synthesized from *trans*-$[RuPy_4(NO_2)_2]$ precursor by the reaction with HCl, HBr or $HClO_4$ [38]. An alternative way is the treatment of *trans*-$[RuNOPy_4OH]^{2+}$ by the corresponding hydrohalic acid, as applied earlier [33,39] and in the present work.

Two crystal modifications *trans*-$[RuNOPy_4F](PF_6)_2 \cdot 0.33H_2O$ (**RuF**) and *trans*-$[RuNOPy_4F](PF_6)_2 \cdot 1.5CH_3CN$ were obtained after recrystallization from water and acetonitrile solvents, respectively (see Experimental). Both crystal structures were measured at 150 K. According to powder XRD (see Fig. S1), the phase *trans*-$[RuNOPy_4F](PF_6)_2 \cdot 1.5CH_3CN$ is stable only in the solution, while when taken out from solvent changes to *trans*-$[RuNOPy_4F](PF_6)_2 \cdot 0.33H_2O$. Since stable bulk material was obtained only for *trans*-$[RuNOPy_4F](PF_6)_2 \cdot 0.33H_2O$ (**RuF**), its structure is described in detail further. The structure of *trans*-$[RuNOPy_4F](PF_6)_2 \cdot 1.5CH_3CN$ and its interatomic distances are given in the supplementary material, in Fig. S2 and Table S2, respectively.

The structure of **RuF** comprises three crystallographically independent ruthenium units *trans*-$[RuNOPy_4F](PF_6)_2$ and one solvent water molecule (see Fig. 1). The ruthenium atom forms an octahedron with *trans*-arrangement of fluoride and nitrosyl ligands. Pyridine ligands are in equatorial plane. Ru3/Ru3A unit exhibits structural disorder of *trans*-F-Ru-N-O chain with occupancies of 0.67 and 0.33, respectively. The disorder contributes larger error to the determination of interatomic distances, which are listed in Table 1. Mostly, the intermolecular interactions are formed by the P-F···H hydrogen bonds, each nitrosyl ligand forms two contacts with fluoride atoms of PF_6^- as illustrated in Fig. 1.

Comparing interatomic distances of *trans*-[RuNOPy$_4$X](PF$_6$)$_2$ (X = F$^-$, Cl$^-$, Br$^-$, OH$^-$) compounds, a considerable difference can be found only in Ru-X bond distances, which are 1.906, 2.322, 2.466, 1.910 Å for F$^-$, Cl$^-$, Br$^-$, OH$^-$, respectively (see Table S3). Note that the crystal data of **RuF**, **RuCl**, **RuBr** and **RuOH** were obtained at different temperatures (150, 180, 180 and 293 K, respectively), so for absolute comparison of distances between these compounds and the correlation of physical properties a corresponding small corrective factor has to be taken into account.

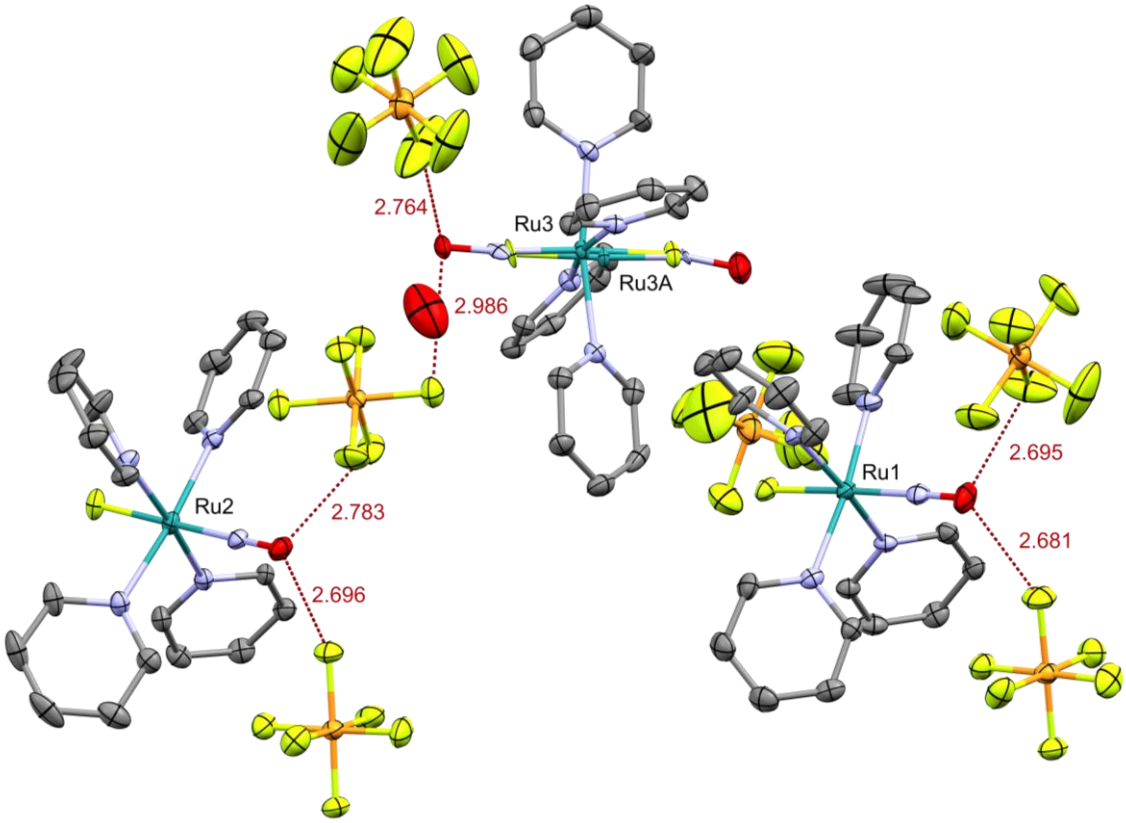

Fig. 1. The structure of *trans*-[RuNOPy$_4$F](PF$_6$)$_2$·0.33H$_2$O (**RuF**) with depicted chosen intermolecular contacts. Hydrogen atoms are omitted for clarity. Thermal ellipsoids are given at the 30% probability level.

Table 1. Chosen interatomic distances [Å] and angles [°] in **RuF**.

	Ru1 unit	Ru2 unit	Ru3/Ru3A unit*
Ru-NO	1.731(8)	1.733(6)	1.74(3)/1.73(3)
N-O	1.14(1)	1.145(9)	1.15(3)/1.16(4)
Ru-F	1.902(4)	1.910(4)	1.90(2)/1.91(3)
Ru-N$_{Py}$	2.082(5); 2.088(5); 2.099(6); 2.089(5)	2.092(6); 2.092(5); 2.082(5); 2.087(5)	2.149(6)/2.089(7); 2.116(5)/2.215(7); 2.075(5)/2.143(6); 2.109(6)/2.023(7)

Ru-N-O	178.2(6)	177.1(5)	169(1)/168(3)
* The two values corresponds to the part of (ON-Ru-F) group with atomic occupancy of 0.67 (Ru3) and0.33 (Ru3A), respectively.			

Spectroscopic features of linkage isomers

The characteristic infrared range of the ν(NO) stretching vibration of GS, MS1 and MS2 isomers in $\{RuNO\}^6$ complexes is 2000-1500 cm^{-1} [10,20] . The energy of those bands is gradually downshifted in the sequence GS-MS1-MS2 with corresponding approximate wavenumbers of 1900-1750-1600 cm^{-1}, respectively.

The positions of the *ν*(NO) bands of GS of studied compounds at 100 K are listed in Table 2 and shown in Fig. 2. The halide compounds exhibit higher energies of the *ν*(NO) band, which are shifted with respect to **RuOH** by about 30 cm^{-1}. It is known that the *ν*(NO) band of the hydroxyl complexes with pyridine ligands possess energy about 1850 cm^{-1} [38,40,41], which is associated with a *trans*-influence of OH^-, but not with the N-O bond distance (see Table S3). Another feature is a splitting of the *ν*(NO) bands of **RuF** complex due to the presence of symmetry-independent ruthenium fragments in the structure, as shown in Fig. 1. This effect is also observed in **RuCl**, which has two symmetry-independent cations in the structure [27].

In order to efficiently generate Ru-ON isomers (MS1) for each compound, LEDs with different wavelengths in the range 365 – 1050 nm were tested. The spectra for the wavelengths which are the most efficient for high MS1 populations - 420 nm for **RuF** and **RuOH**, 470 nm for **RuCl** and 505 nm for **RuBr** - are shown in Fig. 2. The $\nu(NO)_{MS1}$ bands at ≈1750 cm^{-1} are downshifted by ≈150 cm^{-1} compared to $\nu(NO)_{GS}$ and possess features similar to those of $\nu(NO)_{GS}$ bands, namely the relative position depending on **X** and splitting. The photo-generation of MS2 was performed by a subsequent irradiation of MS1 by 940 or 1050 nm (see Fig. 2). The $\nu(NO)_{MS2}$ bands are downshifted by ≈300 cm^{-1} compared to $\nu(NO)_{GS}$ (Table 2). Note that $\nu(NO)_{MS2}$ bands are overlapped with *ν*(C-C) bands of pyridines at ≈1600 cm^{-1}, and for **RuCl** and **RuBr** complexes appear as shoulders to those bands. The populations of metastable states were calculated based on the intensity of $\nu(NO)_{GS}$ bands before and after irradiation using the formula $\%_{MS} = 100 - (I(\nu(NO)_{GS\ after})/I(\nu(NO)_{GS\ before}))\cdot 100$, and shown in Table 2. According to measured populations, reachable amount of MS1 in **RuF**, **RuCl** and **RuOH** is higher than in **RuBr** and related to the features of absorption bands of MS1 discussed below. It's worth mentioning that populations of **RuCl** and **RuBr** measured by IR-spectroscopy are similar to those reported earlier [20,29]. Finally, red light irradiation (650 nm) of both MS1 and MS2 reversibly switches metastable states back to GS in all studied compounds.

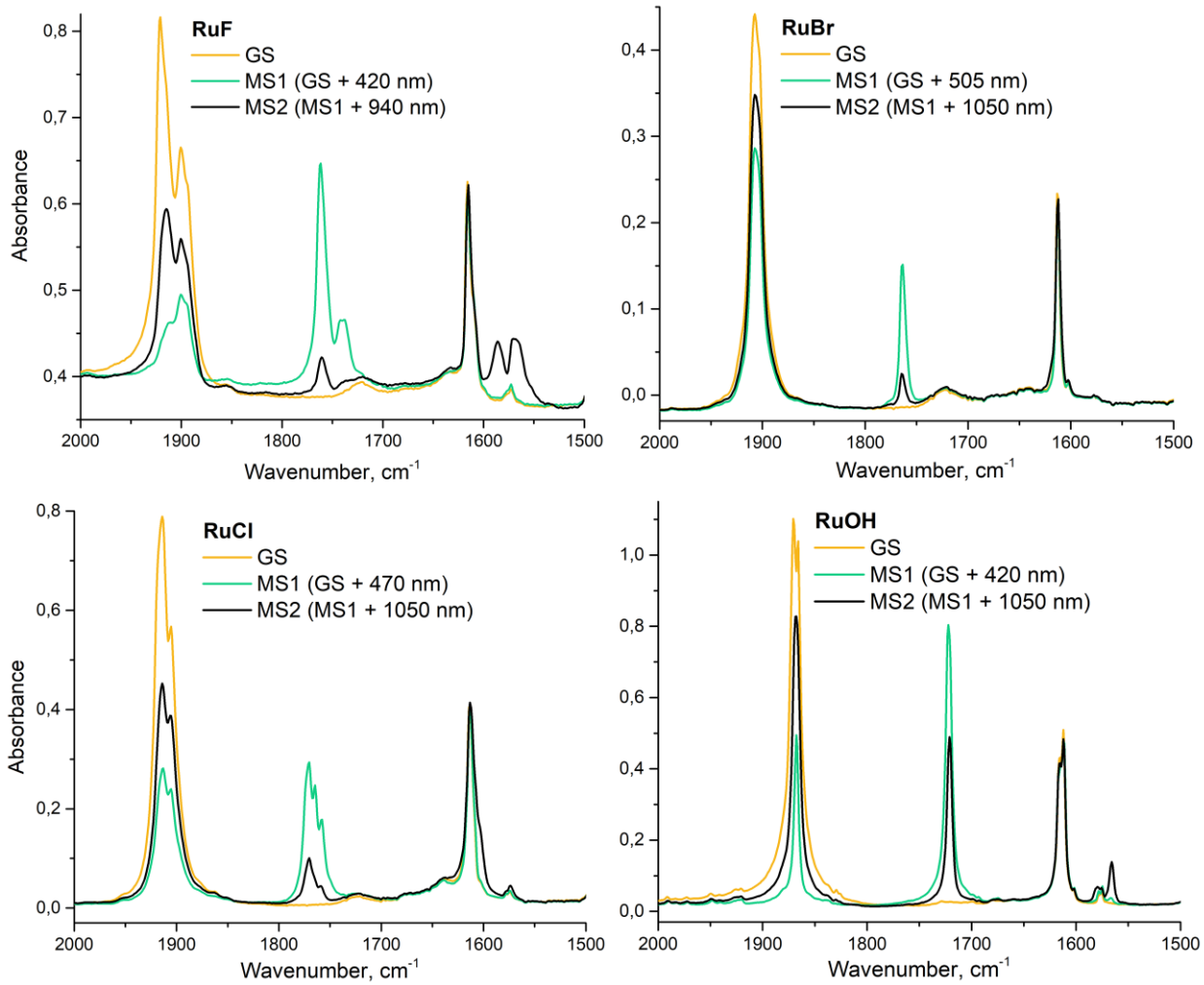

Fig. 2. IR spectra of studied complexes in GS, MS1 and MS2 at 100 K.

Table 2. Bands of GS, MS1 and MS2.

	GS	MS1		MS2	
	ν(NO), cm^{-1}	ν(NO), cm^{-1}	%	ν(NO), cm^{-1}	%
RuF	$1921/1915_{sh}/1901/1893_{sh}$	1762/1742/1738	77	$1586/1571/1566_{sh}$	33
RuCl	$1918_{sh}/1914/1905$	$1774_{sh}/1770/1765/1758$	62/76*	$1618_{sh}/1605_{sh}/1572_{sh}$	36/56*
RuBr	$1907/1903_{sh}$	1764	38/46*	$1618_{sh}/1609_{sh}$	20/18*
RuOH	1871/1866	1722	78	$1581_{sh}/1566$	9
* Values are taken from ref. [20,29].					

Besides the *ν*(NO) vibration, most of the other vibrational bands are also shifted due to the structural reorganization after NO ligand photo-isomerization. In case of **RuOH**, stretching *ν*(OH) and bending δ(OH) vibrations of the hydroxyl ligand are shifted from 3370 and 952 cm^{-1} in GS to 3320 and 1001 cm^{-1} in MS1, respectively.

The changes in the low energy range of the spectra (700-400 cm^{-1}) are listed in Table 3 and shown in Fig. S3. The *ν*(Ru-(NO)) and δ(Ru-(N-O)) modes cannot be resolved and hence these bands are assigned to the same energy. Recently it was shown for $[RuNOPy_4F]^{2+}$ cation that *ν*(Ru-(NO)) and δ(Ru-(N-O)) modes in GS may have merely the same energy, but are essentially split in case of MS1 and MS2 [42]. NO isomerization leads to the downshift of *ν*(Ru-(NO)) and δ(Ru-(N-O)) vibrations in case of MS1 for about 125 cm^{-1} compared to GS, while the downshift of *ν*(Ru-(NO)) is relatively larger. In **RuF** the *ν*(Ru-(NO)) mode of MS2 is downshifted as well, whereas δ(Ru-(N-O)) energies of MS2 of **RuOH** and **RuCl** are much closer to those of GS, which is expected from calculations [42]. Since the Ru-X bond length is decreased after NO ligand isomerization [10,27], the energy of the corresponding *ν*(Ru-X) mode is increased. In case of **RuOH** the bands at 642 and 668 cm^{-1} are tentatively assigned to the *ν*(Ru-OH) mode of GS and MS1 respectively. Besides of X-Ru-(NO) chain, stretching and bending vibrations of pyridine rings are slightly downshifted in MS1.

Table 3. Low energy IR bands of GS, MS1 and MS2 [cm^{-1}].

		$Py_{ring\ stretch}$	*ν*(Ru-(NO))	δ(Ru-(N-O))	*ν*(Ru-X)	$Py_{ring\ bend}$
RuF	GS	659/649	626	626	570_{sh}	462/447
	MS1	656	482/472	510	618	442/430
	MS2	-	419	-	590	-
RuCl	GS	653	606	606	-	482/456
	MS1	-	482/468	-	-	-
	MS2	-	-	586	-	-
RuBr	GS	652	596	596	-	483/471/452
RuOH	GS	654	595	595	642	471/461/447
	MS1	633	487	504	668	435
	MS2	-	-	608	-	-

Absorption properties of GS, MS1 and MS2 in UV-vis range provide important information on population-depopulation efficiency of linkage isomers [43,44]. Since the mechanism of nitrosyl ligand photo-isomerization is a two-stage process and can be schematically described as GS→MS2→MS1 [10,19,21,22], MS1 generation is possible in case of sufficient cross section of GS and MS2 bands at light excitation wavelength. Further, the reachable population of MS1 is determined by the cross section of MS1 at irradiation wavelength, hereby higher cross section induces higher probability of MS1 excitation back to GS and MS2 and leads to lower MS1 population.

The UV-vis absorption spectra of the studied compounds in GS, MS1 and MS2 are shown in Fig. 3. In GS, bands corresponding to the transitions from ruthenium *d* orbitals to unoccupied orbitals of Ru-NO bond appear at around 420, 450, 470 and 430 nm for **RuF**, **RuCl**, **RuBr** and **RuOH**, respectively. Irradiation of the compounds by blue light at 100 K leads to the formation of bands in UV and red spectral range corresponding to transitions of the MS1

isomer. The low energy bands of MS1 (660, 770 (782 [20]), >800, 650 nm for **RuF**, **RuCl**, **RuBr** and **RuOH**, respectively) are downshifted by about 200-300 nm with respect to the low energy bands of GS, thus the HOMO-LUMO gap is decreased by about 1 eV. Regarding MS2, absorption maxima are found at 520, 550 (562 [20]) and 590 nm for **RuF**, **RuCl** and **RuBr**, while the low MS2 population in **RuOH** prevents the detection of that band. Recalling that MS1 is generated via a two-step mechanism with MS2 as intermediate step, we can make the following observations. First, the large separation of absorption bands of GS and MS1 favors high MS1 populations, since in this case in the photostationary state the excitation wavelength will not result in back transfer from MS1 to GS, unless there is a higher lying transition downshifted from UV which would result in such a back transfer. Second, there must be significant overlap between GS and MS2 absorption bands in order to guarantee an efficient forward process GS→MS2→MS1. These conditions are fulfilled in all studied compounds, as illustrated by the difference spectra of MS1 and GS (see Fig. S4), which exhibit characteristic minima for each compound: 420, 460, 490 and 430 nm for **RuF**, **RuCl**, **RuBr** and **RuOH**, respectively, which are similar to the wavelengths responsible for the highest found MS1 population: 420, 470, 505, 420 nm, respectively. Thus, generation of MS1 by light with higher or lower wavelength leads to a decrease of reachable MS1 population due to higher efficiency of the reverse transformation to GS/MS2. The relatively lower MS1 population in **RuBr** can be explained by a relatively lower decrease of MS1 absorption at the excitation wavelength, inducing more efficient back transfer to GS/MS2 (see Fig. 3 and Fig. S4).

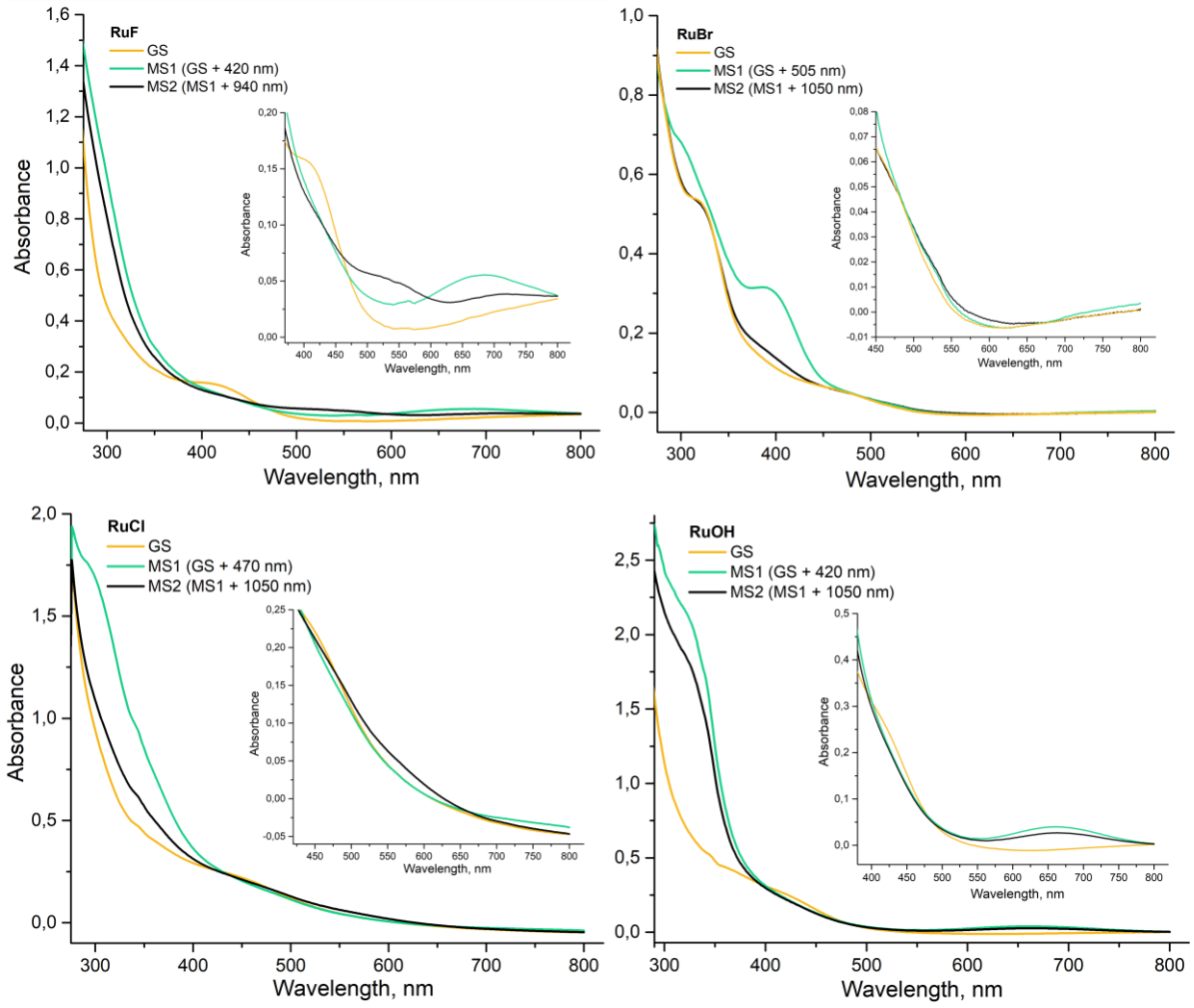

Fig. 3. UV-vis spectra of studied compounds in GS, MS1 and MS2 at 100 K.

Thermal stability of linkage isomers

The thermal stability of linkage isomers was studied by differential scanning calorimetry (DSC) or IR-spectroscopy. Measured DSC curves (see Fig. 4) were fitted by the first order kinetics $dH/dt = H_{tot}\cdot(1-\alpha)k_0\cdot\exp(-E_a/(R\cdot T))$, where dH/dt is heat flow rate, H_{tot} is total reaction enthalpy, α is conversion, E_a is activation energy, k_0 is frequency factor, R is universal gas constant, and T - temperature. The thermal decay of MS2 in **RuOH** and **RuBr** was measured by IR-spectroscopy (see Experimental) due to the rather low temperature at which the exothermic MS2⟶GS reaction occurs, which restricts the usage of DSC method. Kinetic data obtained by DSC and IR-spectroscopy are comparable which was shown recently [33]. The kinetic parameters of decay of MS1 and MS2 in **RuCl** were taken from earlier work [20]. A useful parameter to compare thermal stability of metastable states of different complexes is the decay temperature T_d, where the rate constant $k = 10^{-3}$ s^{-1} roughly corresponds to the onset temperature on the DSC curve [45]. Calculated E_a, k_0 and T_d are shown in Table 4.

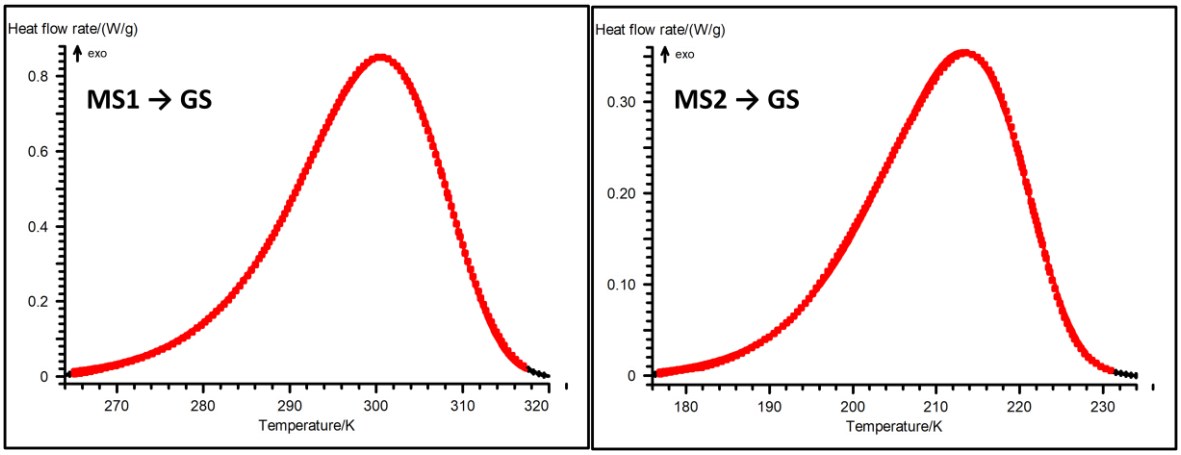

Fig. 4. DSC curves of MS1 and MS2 decay for **RuF** complex.

Table 4. Thermal stability of MS1 and MS2.

	MS1			MS2		
	E_a, kJ mol^{-1}	lgk_0	T_d, K	E_a, kJ mol^{-1}	lgk_0	T_d, K
RuF	89.1±0.4	13.7±0.1	279	43.2±0.2	8.8±0.1	191
RuCl*	67.5±2.9	12.3	231	36.7±2.9	9.8	150
RuOH	73.4±0.1	14.3±0.1	222	21.6±4.1	4.9±1.4	143
RuBr	65.5±0.4	14.0±0.1	201	22.6±1.1	6.0±0.4	131
* Data from [20]						

As can been seen from Table 4, T_d of both MS1 and MS2 are decreased in the sequence **RuF**, **RuCl**, **RuOH**, **RuBr**. According to previous investigations, thermal stability of MS1 depends on the electronegativity of *trans*-ligand to NO (**X**), where higher electronegativity increases the decay temperature [33,39,46]. According to current work, higher electronegativity of **X** is as well responsible for a higher thermal stability of the MS2 isomer. Linear fits of Mulliken electronegativity of **X** vs. decay temperatures of MS1 and MS2 are shown in Fig. 5, *a*. To provide an additional parameter for a prediction of thermal stability of linkage isomers, Hirshfeld charges of the isomeric structures were calculated using DFT approach. Hirshfeld charge is a convenient measure to estimate local electron density on the atoms [47–49]. Similar to Mulliken electronegativity, Hirshfeld charges on RuNO, **X** or on **X-Py$_4$** in MS1 and MS2 correlate with decay temperatures of MS1 and MS2 (see Fig. 5, *b* and Fig. S6, S7). However, if charges of **RuF**, **RuCl** and **RuBr** almost linearly correlate with T_d, charges of **RuOH** are slightly out of linear dependence. Such behavior can be explained by an intermolecular interaction (hydrogen bond formation) of coordinated hydroxyl ligand with the solvent water molecule in the structure of **RuOH,** indicating that the interactions with the environment might significantly influence the decay temperature. Indeed, in the related complex *trans*-[RuNOPy$_4$OH](ClO$_4$)$_2$ the decay temperature of MS1 is by 10 K lower and reaches 211 K [39]. Generally, the high population of MS1 and MS2 in the studied compounds allows to perform photo-crystallographic investigation of all isomers in order to reveal more detailed structural influence on properties of linkage isomers, which is the aim of further investigation.

It can be noted that the positive charges on the (RuNO) group change in the sequence q(MS1) > q(GS) > q(MS2), and the charges on **X-Py$_4$** fragments logically changes in the opposite sequence q(MS2) > q(GS) > q(MS1). Considering charges on **X** and **Py$_4$** in **X-Py$_4$** fragment, the charge distribution changes differently for GS/MS1 compared to GS/MS2 pairs. Specifically, between GS and MS1, a bigger change of the charges is found on Py ligands, whereas between GS and MS2 a larger change is observed on **X** (see Tables S4, S5). Thus, after NO isomerization charge redistribution occurs not only on the **ON-Ru-X** chain, but in the whole molecule including equatorial (pyridine) ligands. Looking in more detail into this charge redistribution, on the example of **RuF** (see Table S4), we find the following: (i) going from GS to MS1, the (RuNO) and **X** fragment become more positive (0.5913 to 0.632 and -0.2084 to -0.1954), while the **Py$_4$** fragment becomes less positive (1.6145 to 1.5636), i.e. upon GS to MS1 isomerization the **Py$_4$** fragment accepts electrons from the other two fragments; (ii) going from GS to MS2, the **X** and **Py$_4$** fragments become more positive (-0.2084 to -0.1924 and 1.6145 to 1.6318), while the (RuNO) fragment becomes less positive (0.5913 to 0.5604), i.e. upon GS to MS2 isomerization, the **Py$_4$** fragment donates electrons. So, while the **X** fragment donates in both cases more electrons to the other groups in MS1/MS2 compared to GS, the **Py$_4$** fragment changes its behavior from an electron "acceptor" in the GS to MS1 isomerization to an electron "donor" in the GS to MS2 isomerization. The same behavior is observed for the whole series of the compounds. However, note that the mentioned changes of the charges on the different fragments are of the order of 6% or less.

From the theoretical work by Yamaletdinov on MS1 thermal stability in a series of [RuNO(NH$_3$)$_4$X]$^{2+}$ compounds [46], thermal stability (activation energy) of MS1 is connected with a charge transfer from **X** to unoccupied orbitals of (Ru-ON). Namely, a higher electronegativity of **X** diminishes the charge transfer to (Ru-ON) increasing the energy

of a transition state of MS1→GS process. From the Hirshfeld charge analysis point view, physical meaning of the increase in the charge on (RuNO) is the increase in activation barrier or thermal stability of the metastable state due to less efficient charge transfer from **X**. Since Hirshfeld charges on **X**, (RuNO) or **X-Py$_4$** groups in GS also correlate with decay temperatures of MS1 and MS2 (see Fig. S8-S10), and well correlate with **X**, (RuNO) or **X-Py$_4$** charges of MS1 or MS2 (see Fig. S11-13), the charges from any isomer can be used for a qualitative prediction of thermal stability of both metastable states. However, while this correlation holds quite nicely within the family of investigated compounds where only the trans-to-NO ligand **X** was varied, further studies will be needed before more general quantitative predictions might be put forward, since besides of **X**, there is an influence of equatorial ligands and second coordination sphere by means of intermolecular contacts [50].

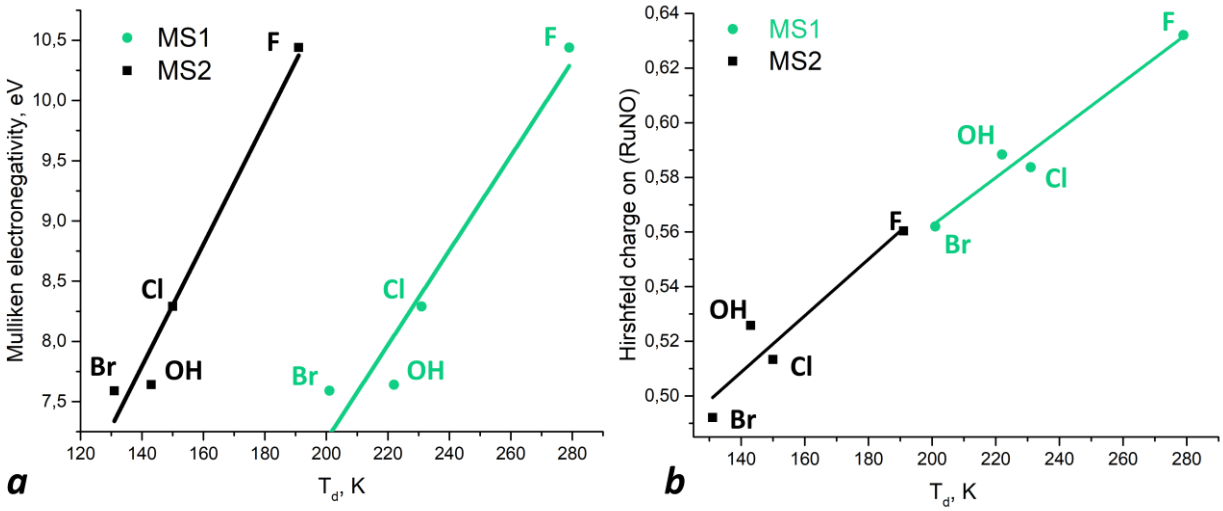

Fig. 5. *a*: dependence of T_d of MS1 and MS2 from Mulliken electronegativity of *trans*-ligand to NO (**X**) with corresponding linear fit; *b*: correlation of Hirshfeld charge on (RuNO) group in MS1 and MS2 with decay temperatures (T_d) of MS1 and MS2, respectively.

Conclusions

Spectroscopic and thermal properties of linkage isomers MS1 and MS2 in the series *trans*-[RuNOPy$_4$X](PF$_6$)$_2$ (X = F$^-$ (**RuF**), Cl$^-$ (**RuCl**), Br$^-$ (**RuBr**) and OH$^-$ (**RuOH**)) were investigated to reveal the influence of *trans*-to NO ligand (**X**). All compounds exhibit a high population of MS1 (about 50-80%) and MS2 (about 10-60%). The HOMO-LUMO gap is increased in the sequence **RuBr** < **RuCl** < **RuOH/RuF** (2.6-3 eV) in GS and decreased with the same sequence in MS2 by ≈0.5 eV (2.1-2.4 eV) and MS1 by ≈1 eV (1.5-1.9 eV). The major difference in GS isomer structures is observed in the Ru-X bond lengths, which are 1.906, 2.322, 2.466, 1.910 Å for X = F$^-$, Cl$^-$, Br$^-$, OH$^-$, respectively. The Ru-X bond lengths of halide compounds correlate well with MS1/MS2 decay temperatures (T_d), whereas **RuOH** complex does not match the linear correlation, thus considering solely interatomic distances cannot be used for the estimation of T_d. A much better linear fit is observed for the correlation of T_d with Mulliken electronegativity of **X**, which is consistent with recent DFT calculations [46]. The analysis of Hirshfeld charges in GS, MS1 and MS2 shows similar

dependence of thermal stability for both MS1 and MS2 against (RuNO) charge, making this parameter suitable for a qualitative prediction of T_d. The largest deviations from the dependencies are observed for **RuOH** compound, which can be related to the intermolecular interaction of OH^- ligand with water molecule in the crystal structure. Apparently, similar intramolecular patterns influence thermal behavior of both metastable states, which, however, can be modified by the different intermolecular interactions, due to different coordination types of MS1 and MS2. Since the investigated compounds show sufficiently high populations of metastable states, they are good candidates for further photo-crystallographic investigation to unravel influence of intermolecular interactions on the thermal stability of linkage isomers.

Acknowledgements

The work has been supported by grant of Russian Science Foundation (22-43-09001, https://rscf.ru/project/22-43-09001/) and ANR (grant no. ANR-21-CE30-0045-01) in the part of spectroscopic experiments and DFT calculations. The research was supported by the Ministry of Science and Higher Education of the Russian Federation, N 121031700315-2 in the part of synthesis and characterization of ruthenium complexes. Artem Mikhailov is grateful for financial support from the Metchnikov bourse program 2021. Authors thank Aleksandr S. Sukhikh for the measurement of X-ray diffraction of **RuF** single crystal on XRD Facility of NIIC SB RAS.

References

1 A. A. Cordones, J. H. Lee, K. Hong, H. Cho, K. Garg, M. Boggio-Pasqua, J. J. Rack, N. Huse, R. W. Schoenlein and T. K. Kim, *Nat. Commun.*, 2018, 9, 1989.

2 A. Y. Kovalevsky, K. A. Bagley and P. Coppens, *J. Am. Chem. Soc.*, 2002, **124**, 9241–9248.

3 S. B. Vittardi, R. Thapa Magar, D. J. Breen and J. J. Rack, *J. Am. Chem. Soc.*, 2021, **143**, 526–537.

4 D. V. Fomitchev, K. A. Bagley and P. Coppens, *J. Am. Chem. Soc.*, 2000, **122**, 532–533.

5 D. Schaniel, T. Woike, B. Delley, C. Boskovic and H.-U. Güdel, *Phys. Chem. Chem. Phys.*, 2008, **10**, 5531.

6 M. R. Warren, S. K. Brayshaw, A. L. Johnson, S. Schiffers, P. R. Raithby, T. L. Easun, M. W. George, J. E. Warren and S. J. Teat, *Angew. Chemie Int. Ed.*, 2009, **48**, 5711–5714.

7 L. E. Hatcher, M. R. Warren, D. R. Allan, S. K. Brayshaw, A. L. Johnson, S. Fuertes, S. Schiffers, A. J. Stevenson, S. J. Teat, C. H. Woodall and P. R. Raithby, *Angew. Chemie - Int. Ed.*, 2011, **50**, 8371–8374.

8 S. E. Bajwa, T. E. Storr, L. E. Hatcher, T. J. Williams, C. G. Baumann, A. C. Whitwood, D. R. Allan, S. J. Teat, P. R. Raithby and I. J. S. Fairlamb, *Chem. Sci.*, 2012, **3**, 1656.

9 S. E. Kutniewska, A. Krówczyński, R. Kamiński, K. N. Jarzembska, S. Pillet, E. Wenger and D.

Schaniel, *IUCrJ*, 2020, **7**, 1188–1198.

10 A. A. Mikhailov, E. Wenger, G. A. Kostin and D. Schaniel, *Chem. – A Eur. J.*, 2019, **25**, 7569–7574.

11 P. Coppens, I. Novozhilova and A. Kovalevsky, *Chem. Rev.*, 2002, **102**, 861–884.

12 D. Schaniel, M. Imlau, T. Weisemoeller, T. Woike, K. W. Krämer and H.-U. Güdel, *Adv. Mater.*, 2007, **19**, 723–726.

13 B. Bourdon, S. Bock, C. Kijatkin, A. Shumelyuk and M. Imlau, *Opt. Mater. Express*, 2018, **8**, 1951.

14 K. Springfeld, V. Dieckmann and M. Imlau, *Photonics Res.*, 2013, **1**, 197.

15 W.-J. Xu, K. Romanyuk, J. M. G. Martinho, Y. Zeng, X.-W. Zhang, A. Ushakov, V. Shur, W.-X. Zhang, X.-M. Chen, A. Kholkin and J. Rocha, *J. Am. Chem. Soc.*, 2020, **142**, 16990–16998.

16 S. Shin, J. Choe, Y. Park, D. Jeong, H. Song, Y. You, D. Seo and J. Cho, *Angew. Chemie Int. Ed.*, 2019, **58**, 10126–10131.

17 C.-K. Chiang, K.-T. Chu, C.-C. Lin, S.-R. Xie, Y.-C. Liu, S. Demeshko, G.-H. Lee, F. Meyer, M.-L. Tsai, M.-H. Chiang and C.-M. Lee, *J. Am. Chem. Soc.*, 2020, **142**, 8649–8661.

18 A. A. Mikhailov, D. V. Khantakova, V. A. Nichiporenko, E. M. Glebov, V. P. Grivin, V. F. Plyusnin, V. V. Yanshole, D. V. Petrova, G. A. Kostin and I. R. Grin, *Metallomics*, 2019, **11**, 1999–2009.

19 L. Khadeeva, W. Kaszub, M. Lorenc, I. Malfant and M. Buron-Le Cointe, *Inorg. Chem.*, 2016, **55**, 4117–4123.

20 D. Schaniel, B. Cormary, I. Malfant, L. Valade, T. Woike, B. Delley, K. W. Krämer and H. U. Güdel, *Phys. Chem. Chem. Phys.*, 2007, **9**, 3717–3724.

21 F. Talotta, J.-L. Heully, F. Alary, I. M. Dixon, L. González and M. Boggio-Pasqua, *J. Chem. Theory Comput.*, 2017, **13**, 6120–6130.

22 F. Talotta, M. Boggio-Pasqua and L. González, *Chem. – A Eur. J.*, 2020, **26**, 11522–11528.

23 J. Sanz García, F. Alary, M. Boggio-Pasqua, I. M. Dixon, I. Malfant and J.-L. Heully, *Inorg. Chem.*, 2015, **54**, 8310–8318.

24 F. Talotta, L. González and M. Boggio-Pasqua, *Molecules*, 2020, **25**, 2613.

25 J. S. García, F. Alary, M. Boggio-Pasqua, I. M. Dixon and J.-L. Heully, *J. Mol. Model.*, 2016, **22**, 284.

26 D. Schaniel, T. Woike, C. Merschjann and M. Imlau, *Phys. Rev. B*, 2005, **72**, 195119.

27 B. Cormary, I. Malfant, M. Buron-Le Cointe, L. Toupet, B. Delley, D. Schaniel, N. Mockus, T. Woike, K. Fejfarová, V. Petříček and M. Dušek, *Acta Crystallogr. Sect. B Struct. Sci.*, 2009, **65**, 612–623.

28 D. Schaniel, T. Woike, C. Boskovic and H. U. Güdel, *Chem. Phys. Lett.*, 2004, **390**, 347–351.

29 B. Cormary, S. Ladeira, K. Jacob, P. G. Lacroix, T. Woike, D. Schaniel and I. Malfant, *Inorg. Chem.*, 2012, **51**, 7492–7501.

30 A. N. Makhinya, M. A. Il'in, R. D. Yamaletdinov, I. A. Baidina, S. V. Tkachev, A. P. Zubareva, I. V. Korol'kov and D. A. Piryazev, *Russ. J. Coord. Chem.*, 2016, **42**, 768–774.

31 H. Nishimura, H. Matsuzawa, T. Togano, M. Mukaida, H. Kakihana and F. Bottomley, *J. Chem. Soc. Dalt. Trans.*, 1990, 137–141.

32 T. Kimura, T. Sakurai, M. Shima, T. Togano, M. Mukaida and T. Nomura, *Inorganica Chim. Acta*, 1983, **69**, 135–140.

33 G. A. Kostin, A. A. Mikhailov, N. V. Kuratieva, D. P. Pishchur and A. N. Makhinya, *New J. Chem.*, 2018, **42**, 18928–18934.

34 G. M. Sheldrick, *Acta Crystallogr. Sect. A Found. Adv.*, 2015, **71**, 3–8.

35 O. V. Dolomanov, L. J. Bourhis, R. J. Gildea, J. A. K. Howard and H. Puschmann, *J. Appl. Crystallogr.*, 2009, **42**, 339–341.

36 G. te Velde, F. M. Bickelhaupt, E. J. Baerends, C. Fonseca Guerra, S. J. A. van Gisbergen, J. G. Snijders and T. Ziegler, *J. Comput. Chem.*, 2001, **22**, 931–967.

37 A. D. Becke, *Phys. Rev. A*, 1988, **38**, 3098–3100.

38 F. Bottomley and M. Mukaida, *J. Chem. Soc. Dalt. Trans.*, 1982, 1933.

39 V. Vorobyev, A. A. Mikhailov, V. Y. Komarov, A. N. Makhinya and G. A. Kostin, *New J. Chem.*, 2020, **44**, 4762–4771.

40 A. N. Makhinya, M. A. Il'in, R. D. Yamaletdinov, I. V. Korolkov and I. A. Baidina, *New J. Chem.*, 2016, **40**, 10267–10273.

41 A. N. Makhinya, M. A. Il'in, E. V. Kabin, I. A. Baidina, M. R. Gallyamov and N. I. Alferova, *Russ. J. Coord. Chem.*, 2014, **40**, 297–303.

42 A. A. Mikhailov, T. Woike, A. Gansmüller, D. Schaniel and G. A. Kostin, *Spectrochim. Acta Part A Mol. Biomol. Spectrosc.*, 2021, **263**, 120217.

43 D. Schaniel and T. Woike, *Phys. Chem. Chem. Phys.*, 2009, **11**, 4298–4359.

44 D. Schaniel, J. Schefer, B. Delley, M. Imlau and T. Woike, *Phys. Rev. B*, 2002, **66**, 085103.

45 Y. Morioka, A. Ishikawa, H. Tomizawa and E. Miki, *J. Chem. Soc. Dalt. Trans.*, 2000, **54**, 781–786.

46 R. D. Yamaletdinov and I. L. Zilberberg, *Eur. J. Inorg. Chem.*, 2017, **2017**, 2951–2954.

47 F. De Proft, C. Van Alsenoy, A. Peeters, W. Langenaeker and P. Geerlings, *J. Comput. Chem.*, 2002, **23**, 1198–1209.

48 F. L. Hirshfeld, *Theor. Chim. Acta*, 1977, **44**, 129–138.

49 C. Fonseca Guerra, J.-W. Handgraaf, E. J. Baerends and F. M. Bickelhaupt, *J. Comput. Chem.*, 2004, **25**, 189–210.

50 A. A. Mikhailov, V. Y. Komarov, A. S. Sukhikh, D. P. Pishchur, D. Schaniel and G. A. Kostin, *New J. Chem.*, 2020, **44**, 18014–18024.

Supplementary Information

The influence of *trans*-ligand to NO to the thermal stability of side-bond coordinated isomer MS2

Artem A. Mikhailov[a], Gennadiy A. Kostin[a], Dominik Schaniel[b]

[a] Nikolaev Institute of Inorganic Chemistry, Siberian Branch of the Russian Academy of Sciences, 3 Acad. Lavrentiev Avenue, Novosibirsk 630090, Russian Federation

[b] Universite´ de Lorraine, CNRS, CRM2, UMR 7036, Nancy 54000, France

Table S1. Experimental and refinement details.

Complex	$[RuNOPy_4F](PF_6)_2 \cdot 0.33H_2O$	$[RuNOPy_4F](PF_6)_2 \cdot 1.5CH_3CN$
Empirical formula	$C_{20}H_{20.67}F_{13}N_5O_{1.33}P_2Ru$	$C_{46}H_{49}F_{26}N_{13}O_2P_4Ru_2$
Formula weight	762.42	1636.00
Temperature/K	150.0	150.0
Crystal system	triclinic	monoclinic
Space group	P-1	$P2_1/c$
a/Å	13.9264(5)	20.7752(13)
b/Å	16.9480(7)	15.3676(9)
c/Å	19.8185(8)	19.9513(9)
α/°	66.7760(10)	90
β/°	79.868(2)	99.0464(15)
γ/°	84.6740(10)	90
Volume/$Å^3$	4230.2(3)	6290.5(6)
Z	6	4
$\rho_{calc}g/cm^3$	1.796	1.727
μ/mm^{-1}	0.782	0.708
F(000)	2264.0	3256.0
Crystal size/mm^3	0.114 × 0.083 × 0.082	0.12 × 0.1 × 0.01
Radiation	MoKα (λ = 0.71073)	MoKα (λ = 0.71073)
2Θ range for data collection/°	3.908 to 55.066	3.362 to 48.854
Index ranges	-18 ≤ h ≤ 18, -22 ≤ k ≤ 22, -25 ≤ l ≤ 25	-24 ≤ h ≤ 24, -17 ≤ k ≤ 17, -22 ≤ l ≤ 21
Reflections collected	63937	61086
Independent reflections	19420 [R_{int} = 0.0459, R_{sigma} = 0.0514]	10293 [R_{int} = 0.1148, R_{sigma} = 0.0769]
Data/restraints/ parameters	19420/29/1184	10293/0/841
Goodness-of-fit on F^2	1.200	1.016
Final R indexes [I>=2σ (I)]	R_1 = 0.0813, wR_2 = 0.1596	R_1 = 0.0579, wR_2 = 0.1342
Final R indexes [all data]	R_1 = 0.0992, wR_2 = 0.1661	R_1 = 0.0928, wR_2 = 0.1575
Largest diff. peak/hole / e $Å^{-3}$	1.57/-1.11	1.05/-0.73

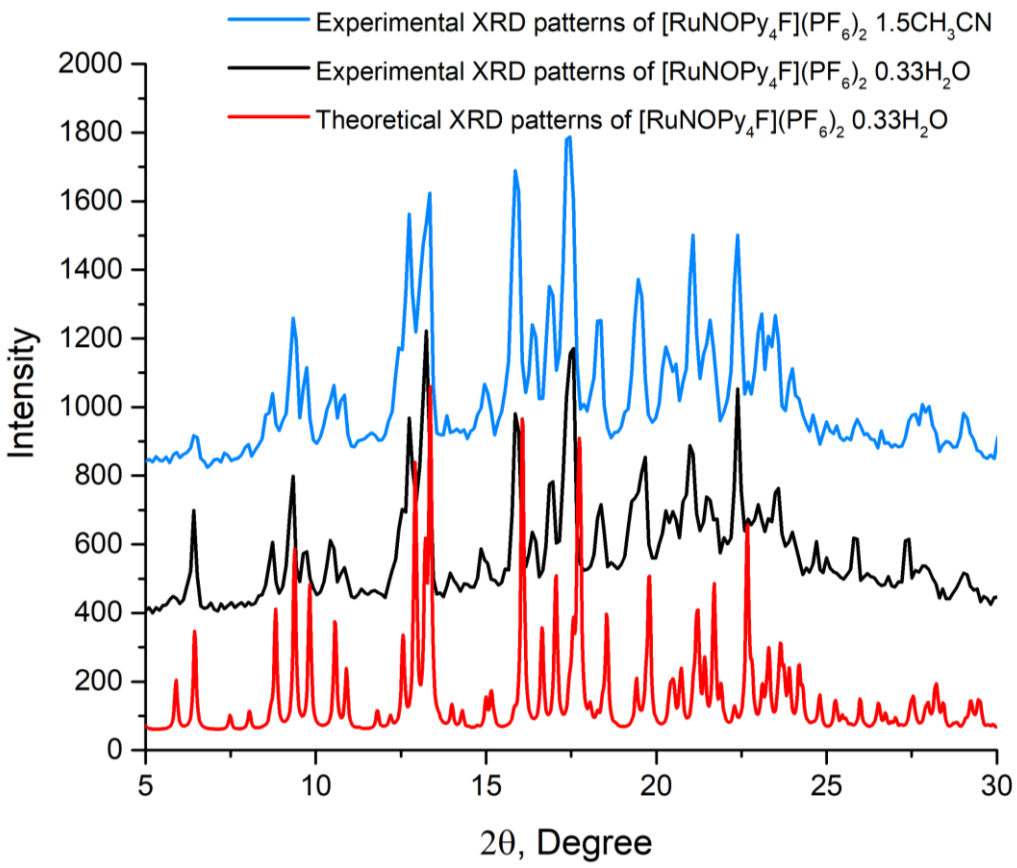

Fig. S1. Comparison of experimental powder XRD patterns of $[RuNOPy_4F](PF_6)_2 \cdot 0.33H_2O$ (**RuF**) and *trans*-$[RuNOPy_4F](PF_6)_2 \cdot 1.5CH_3CN$ with theoretical XRD patterns of $[RuNOPy_4F](PF_6)_2 \cdot 0.33H_2O$ obtained from single crystal XRD.

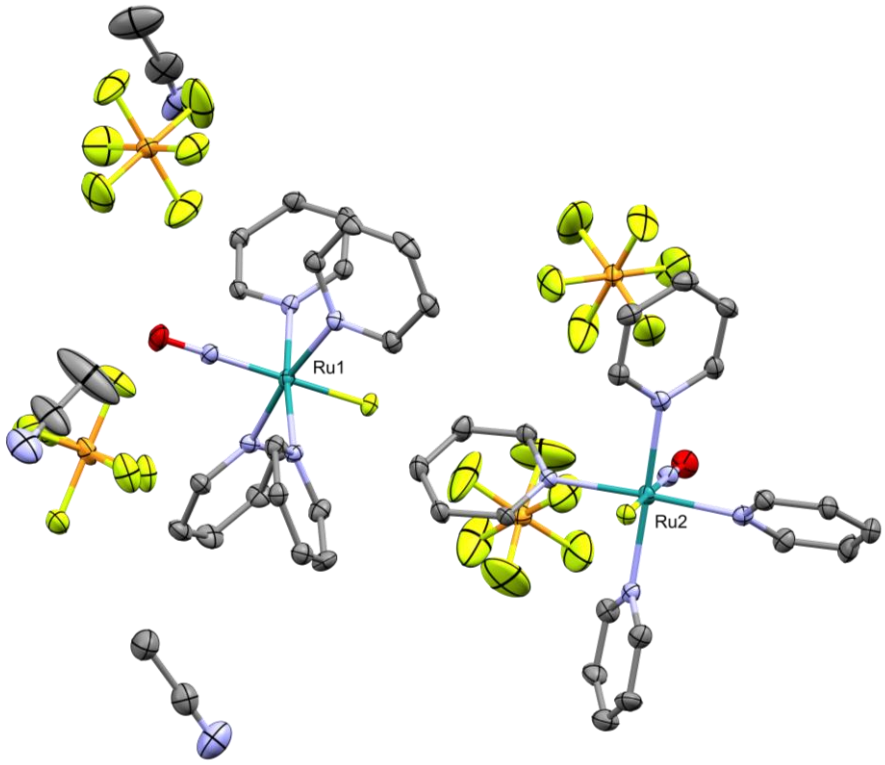

Fig. S2. The structure of *trans*-$[RuNOPy_4F](PF_6)_2 \cdot 1.5CH_3CN$ with two crystallographically independent ruthenium units. Hydrogen atoms are omitted for clarity. Thermal ellipsoids are given at the 30% probability level.

Table S2. Chosen interatomic distances [Å] and angles [°] in *trans*-[$RuNOPy_4F](PF_6)_2 \cdot 1.5CH_3CN$.

	Ru1 unit	Ru2 unit
Ru-NO	1.749(6)	1.730(6)
N-O	1.128(8)	1.142(9)
Ru-F	1.914(3)	1.915(3)
$Ru\text{-}N_{Py}$	2.078(4); 2.091(5); 2.084(6); 2.094(5)	2.094(6); 2.080(6); 2.101(6); 2.100(6)
Ru-N-O	174.0(6)	176.7(6)

Table S3. Chosen bond distances of $[RuNOPy_4X](PF_6)_2$ ($X = F^-$, Cl^-, Br^- and OH^-) complexes. Temperatures of the measurements are indicated in the table (T, K).

	N-O	Ru-NO	Ru-X	$Ru\text{-}Py_{average}$	T, K	Ref.
RuF*	1.14(1); 1.145(9)	1.731(8); 1.733(6)	1.902(4); 1.910(4)	2.089	150	Present work
RuCl	1.146(2); 1.147(2)	1.755(2); 1.754(2)	2.321(1); 2.323(1)	2.108	180	[1]
RuOH	1.145(4)	1.757(3)	1.910(2)	2.103	293	[2]
RuBr	1.131(4)	1.752(3)	2.466(1)	2.108	180	[1]
* In case of **RuF** complex distances of Ru1 and Ru2 units are considered.						

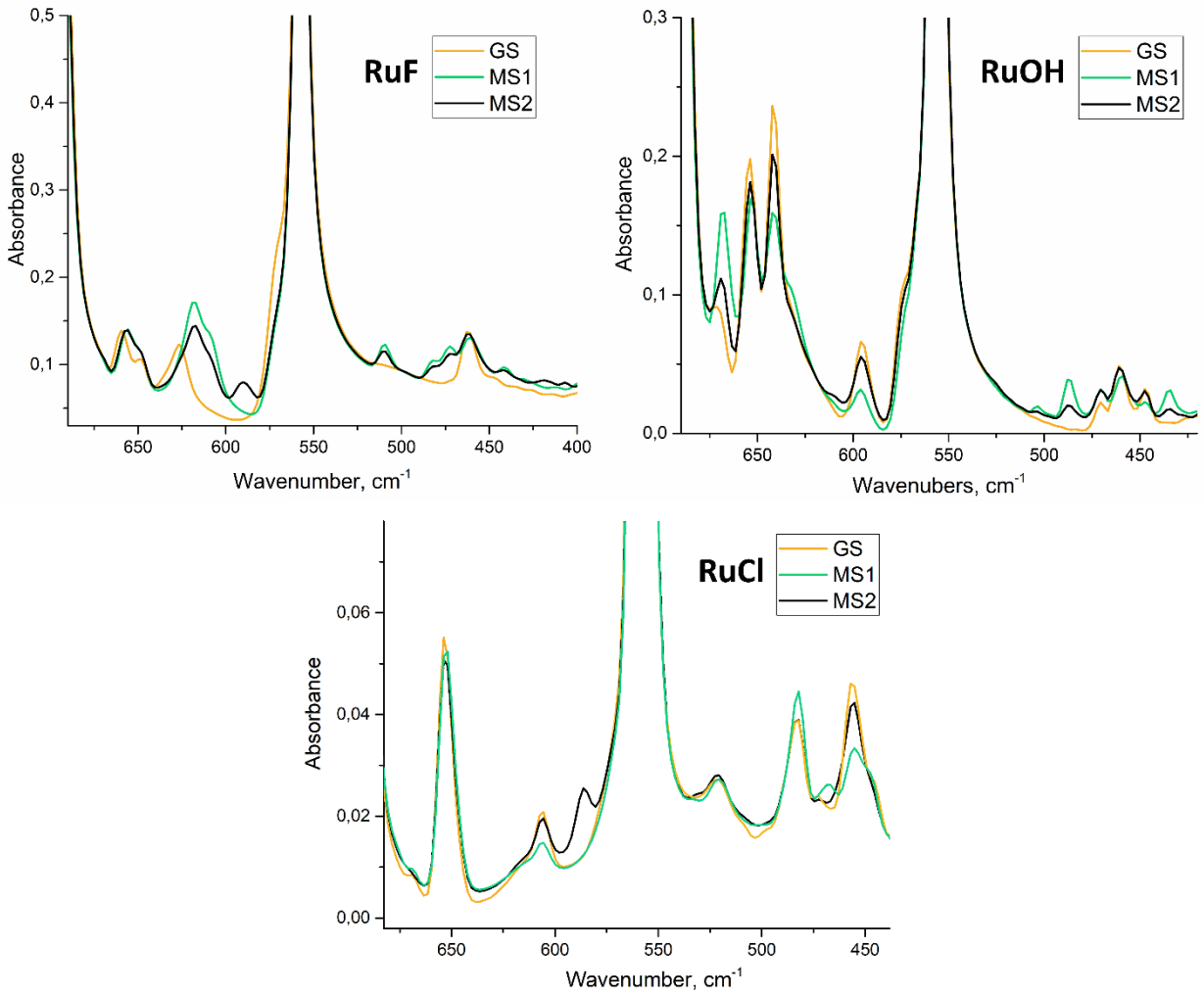

Fig. S3. IR spectra of studied complexes in GS, MS1 and MS2 at 100 K. Strong band at 550 cm^{-1} corresponds to vibration of PF_6^- anion.

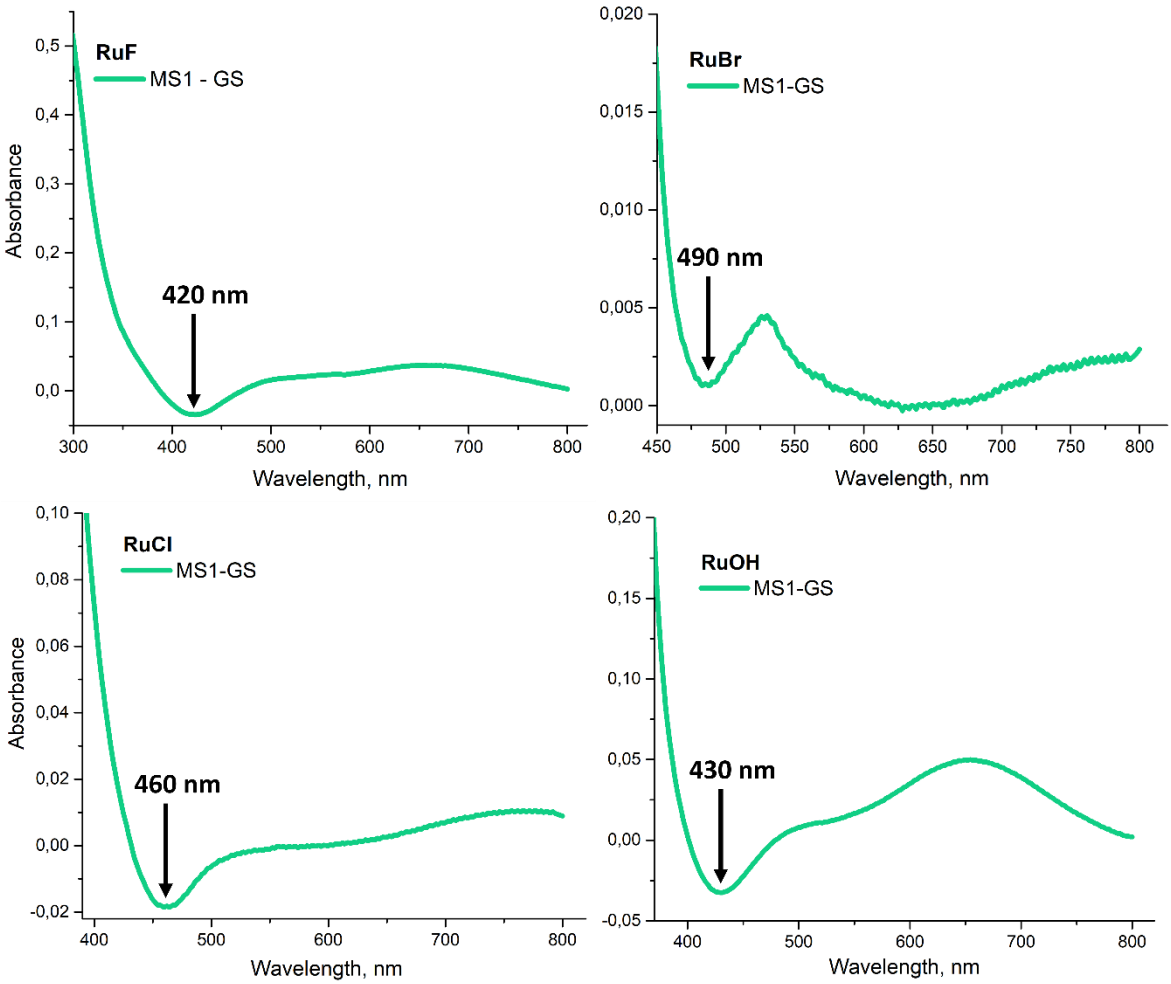

Fig. S4. Difference UV-vis spectra (MS1-GS) of studied compounds at 100 K.

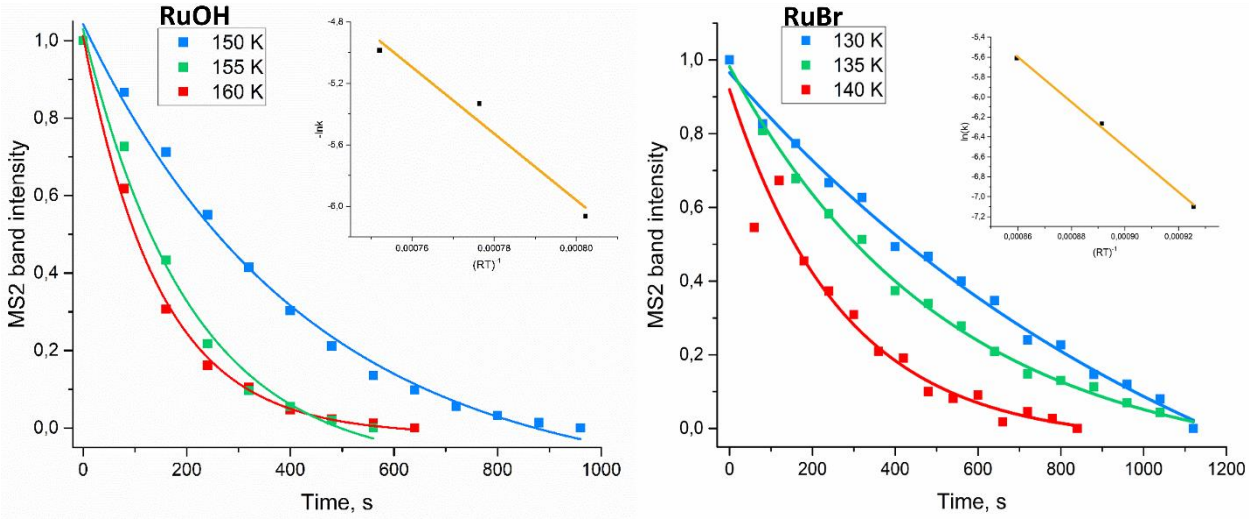

Fig. S5. Isothermal decay of MS2 in **RuOH** and **RuBr** measured by IR-spectroscopy.

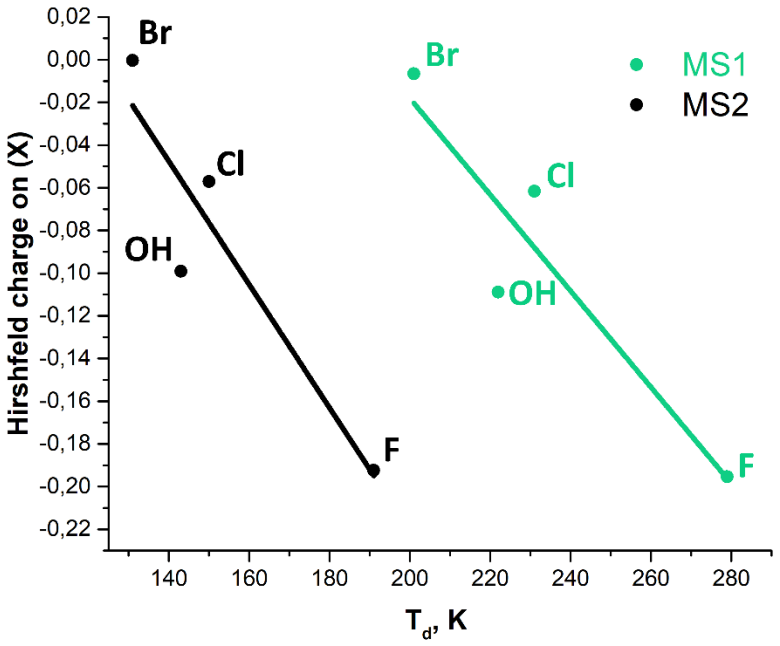

Fig. S6. Correlation of Hirshfeld charge on **X** (NO *trans*-ligand) in MS1 and MS2, and decay temperatures T_d of MS1 and MS2, respectively.

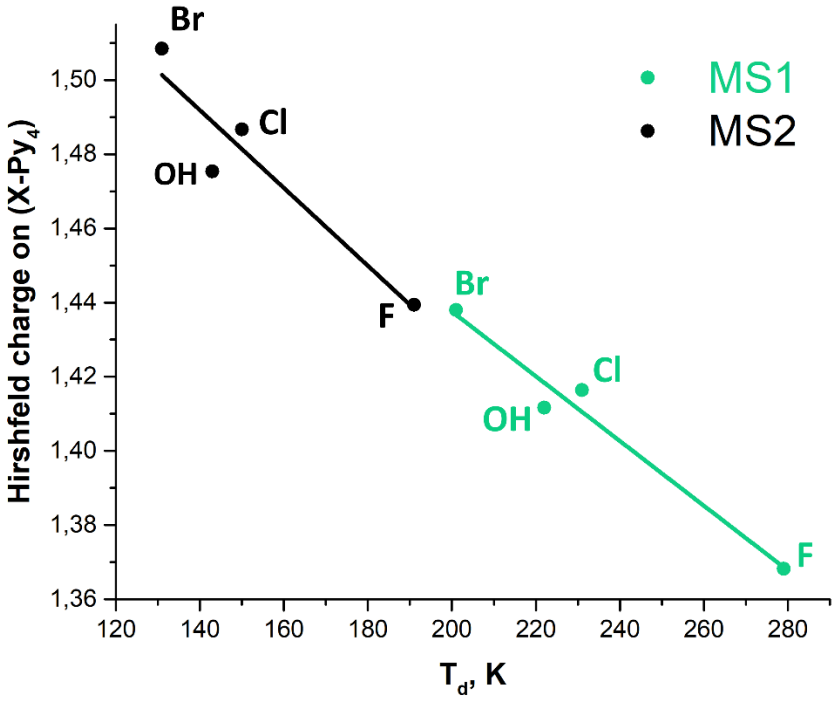

Fig. S7. Correlation of Hirshfeld charge on **X-Py$_4$** in MS1 and MS2, and decay temperatures T_d of MS1 and MS2, respectively.

Table S4. The Hirshfeld charges in GS, MS1 and MS2 on RuNO, X, Py_4 and X-Py_4 groups.

RuNO	GS	MS1	MS2		*X*	GS	MS1	MS2
RuF	0.5913	0.632	0.5604		**RuF**	-0.2084	-0.1954	-0.1924
RuCl	0.5528	0.5837	0.5134		**RuCl**	-0.0931	-0.0616	-0.0571
RuOH	0.5553	0.5883	0.5258		**RuOH**	-0.1276	-0.1089	-0.0991
RuBr	0.5347	0.562	0.4921		**RuBr**	-0.0427	-0.0066	-0.0004
X-Py_4	GS	MS1	MS2		*Py_4*	GS	MS1	MS2
RuF	1.4061	1.3682	1.4394		**RuF**	1.6145	1.5636	1.6318
RuCl	1.4469	1.4164	1.4867		**RuCl**	1.54	1.478	1.5438
RuOH	1.4447	1.4117	1.4754		**RuOH**	1.5723	1.5206	1.5745
RuBr	1.4653	1.438	1.5084		**RuBr**	1.508	1.4446	1.5088

Table S5. The difference of Hirshfeld charges in GS, MS1 and MS2 on RuNO, X, Py_4 and X-Py_4 groups.

RuNO	GS-MS1	GS-MS2		*X*	GS-MS1	GS-MS2
RuF	-0.0407	0.0309		**RuF**	-0.013	-0.016
RuCl	-0.0309	0.0394		**RuCl**	-0.0315	-0.036
RuOH	-0.033	0.0295		**RuOH**	-0.0187	-0.0285
RuBr	-0.0273	0.0426		**RuBr**	-0.0361	-0.0423
X-Py_4	GS-MS1	GS-MS2		*Py_4*	GS-MS1	GS-MS2
RuF	0.0379	-0.0333		**RuF**	0.0509	-0.0173
RuCl	0.0305	-0.0398		**RuCl**	0.062	-0.0038
RuOH	0.033	-0.0307		**RuOH**	0.0517	-0.0022
RuBr	0.0273	-0.0431		**RuBr**	0.0634	-0.0008

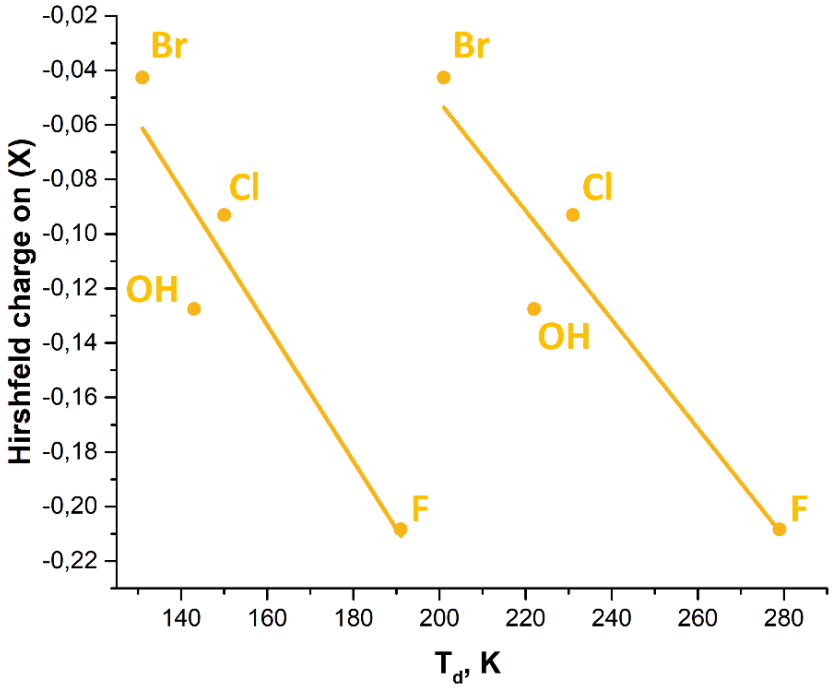

Fig. S8. Correlation of Hirshfeld charge on **X** (NO *trans*-ligand) in GS and decay temperatures T_d of MS1 and MS2.

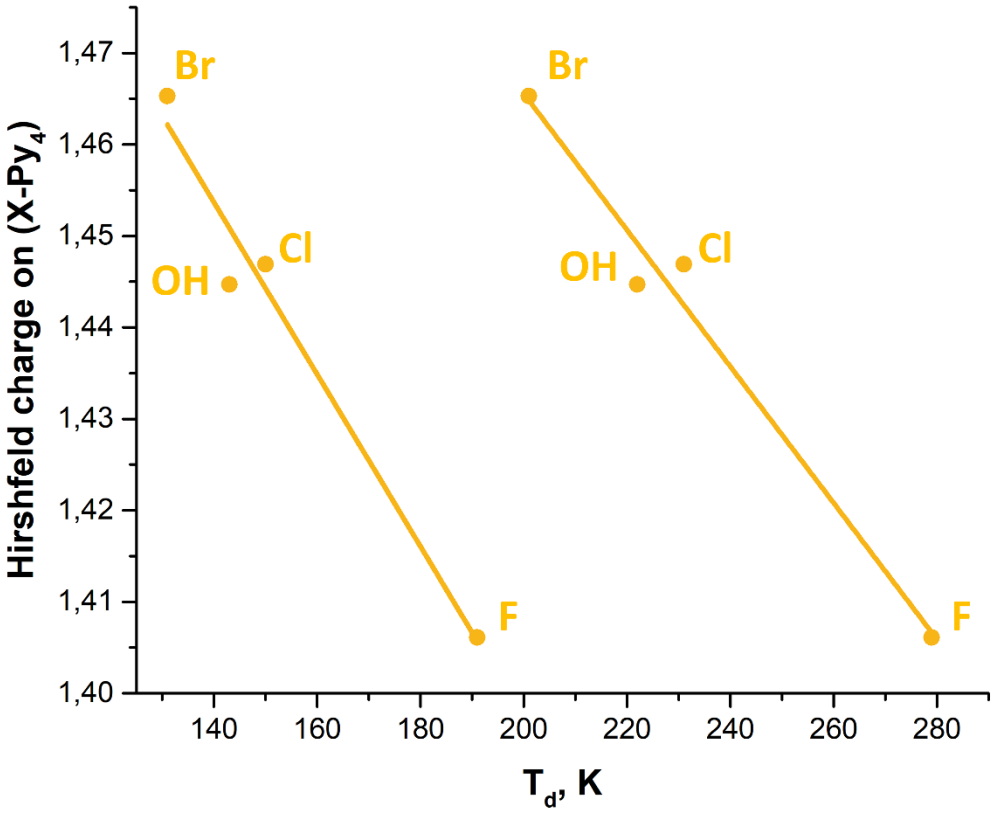

Fig. S9. Correlation of Hirshfeld charge on **X-Py$_4$** in GS and decay temperatures T_d of MS1 and MS2.

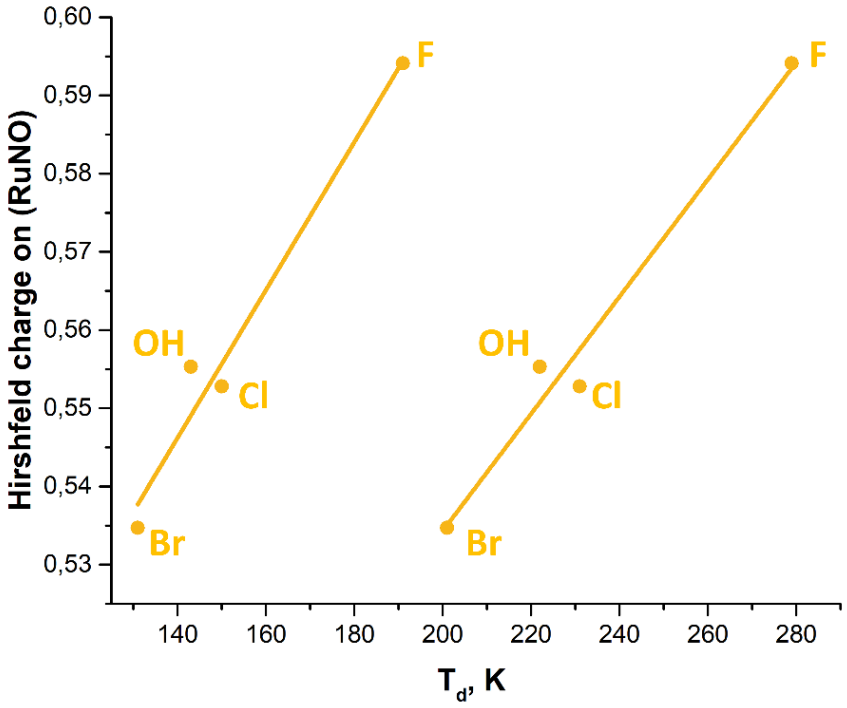

Fig. S10. Correlation of Hirshfeld charge on (RuNO) group in GS and decay temperatures T_d of MS1 and MS2.

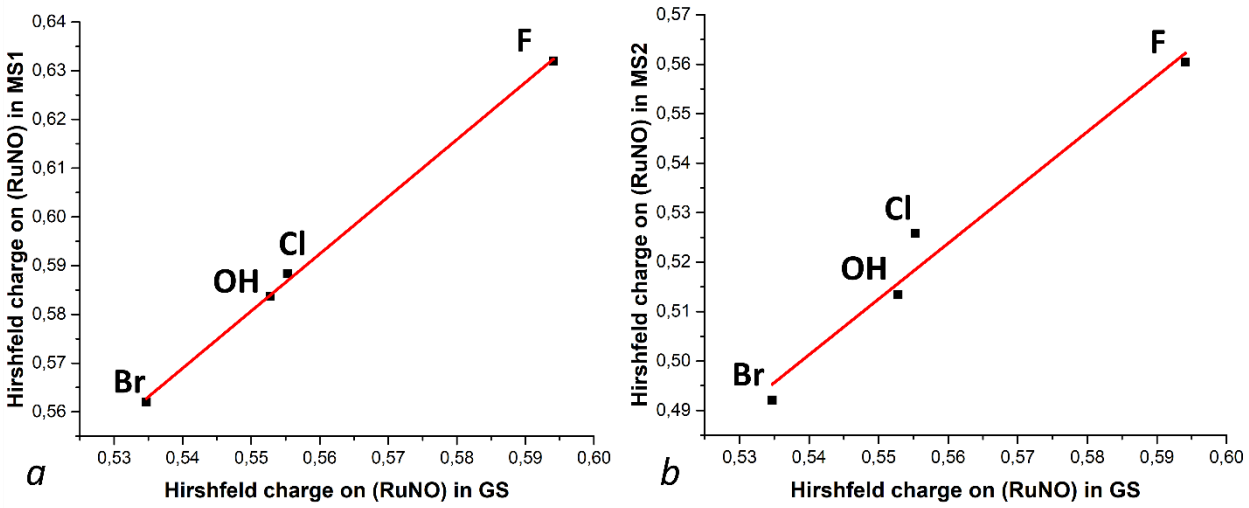

Fig. S11. *a*: correlation of Hirshfeld charges on (RuNO) groups in MS1 and GS; *b*: correlation of Hirshfeld charges on (RuNO) groups in MS2 and GS.

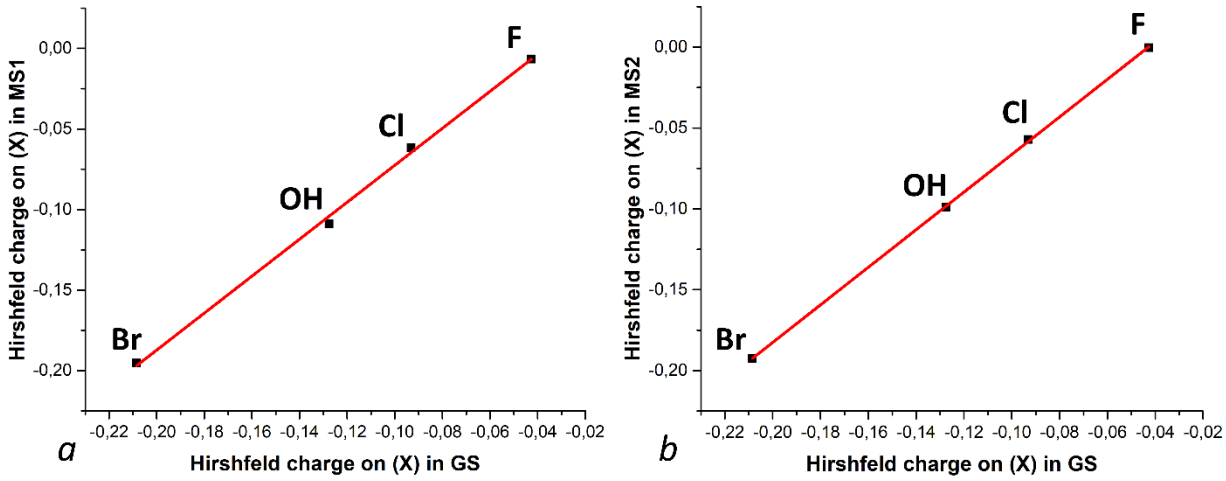

Fig. S12. *a*: correlation of Hirshfeld charges on (**X**) in MS1 and GS; *b*: correlation of Hirshfeld charges on (**X**) in MS2 and GS.

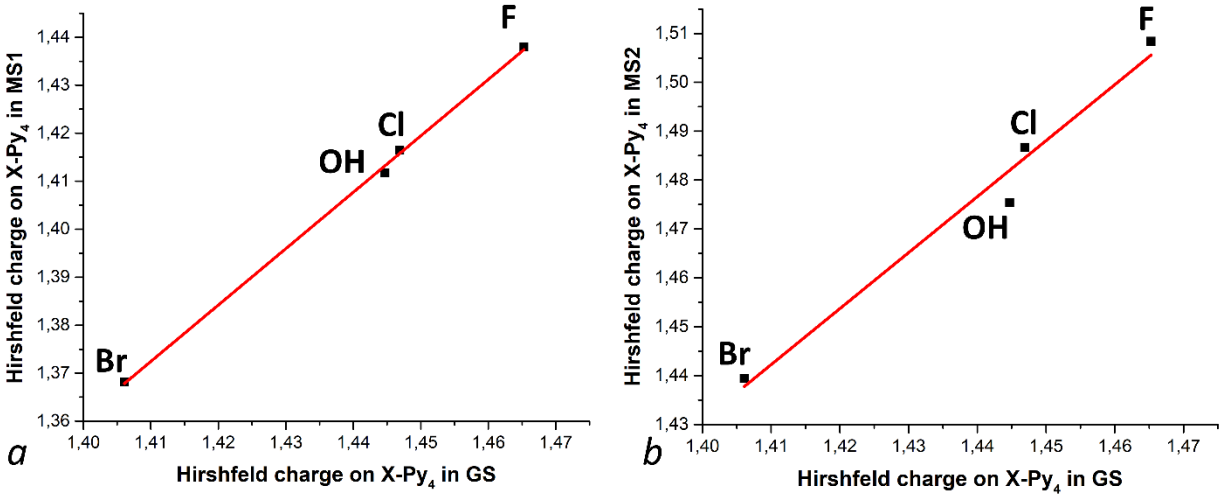

Fig. S13. *a*: correlation of Hirshfeld charges on **X-Py$_4$** in MS1 and GS; *b*: correlation of Hirshfeld charges on **X-Py$_4$** in MS2 and GS.

References

1. Cormary B. et al. Structural Influence on the Photochromic Response of a Series of Ruthenium Mononitrosyl Complexes // Inorg. Chem. 2012. Vol. 51, № 14. P. 7492–7501.

2. Nishimura H. et al. Comparison of the reactivity, electrochemical behaviour, and structure of the trans-bis(acido)tetra(pyridine)nitrosylruthenium cations (acido = hydroxo or chloro) // J. Chem. Soc. Dalt. Trans. 1990. № 1. P. 137.